Spatiotemporally controlled single cell sonoporation

Zhenzhen Fan, Haiyan Liu, Michael Mayer, and Cheri X. Deng[1]

Department of Biomedical Engineering, University of Michigan, Ann Arbor, MI 48109

Edited by Floyd Dunn, University of Illinois, Tucson, AZ, and approved September 5, 2012 (received for review May 15, 2012)

This paper presents unique approaches to enable control and quantification of ultrasound-mediated cell membrane disruption, or sonoporation, at the single-cell level. Ultrasound excitation of microbubbles that were targeted to the plasma membrane of HEK-293 cells generated spatially and temporally controlled membrane disruption with high repeatability. Using whole-cell patch clamp recording combined with fluorescence microscopy, we obtained time-resolved measurements of single-cell sonoporation and quantified the size and resealing rate of pores. We measured the intracellular diffusion coefficient of cytoplasmic RNA/DNA from sonoporation-induced transport of an intercalating fluorescent dye into and within single cells. We achieved spatiotemporally controlled delivery with subcellular precision and calcium signaling in targeted cells by selective excitation of microbubbles. Finally, we utilized sonoporation to deliver calcein, a membrane-impermeant substrate of multidrug resistance protein-1 (MRP1), into HEK-MRP1 cells, which overexpress MRP1, and monitored the calcein efflux by MRP1. This approach made it possible to measure the efflux rate in individual cells and to compare it directly to the efflux rate in parental control cells that do not express MRP1.

intracellular delivery | acoustic cavitation | transmembrane current | mechanical impact

Despite the development of various approaches for transporting membrane-impermeant compounds (such as fluorescent markers, DNA, RNA, siRNA, proteins, peptides, and amino acids) into living cells (1–3), efficient intracellular delivery of bioactive agents for biomedical applications with minimal adverse effects remains challenging. In addition, it is desirable yet difficult to achieve local perturbation of intracellular processes, which requires subcellular molecular localization inside the living cell (4, 5).

Sonoporation uses ultrasound to induce transient disruption of cell membranes (6–8), thereby enabling transport of membrane-impermeant compounds into the cytoplasm of living cells (6, 9–11). Without the need to use viral vectors, sonoporation enables the delivery of a wide range of bioactive agents with minimal inflammatory and immunological responses for both in vitro studies and in vivo applications (12–16). In addition, ultrasound application can be targeted to a specific volume of tissue in vivo noninvasively. These unique characteristics make sonoporation a compelling and versatile technology for nonviral drug and gene delivery.

Sonoporation is typically performed for bulk treatment of a tissue volume in vivo or a large number of cells in vitro, often facilitated by microbubbles that are either injected in the vasculature or mixed in solution with suspended or attached cells. Ultrasound application induces cavitation of the microbubbles (17), signified by rapid volume expansion/contraction and/or collapse (18). These effects generate localized fluid flow, shear stress, and other mechanical or physical impact capable of affecting cells and structures nearby (7, 19, 20).

However, the detailed processes supporting sonoporation-mediated transmembrane and transcellular transport are not well understood, particularly at the single-cell level. The absence of such mechanistic understanding hinders the successful development of the technology as an effective and safe strategy. The main challenge for mechanistic and quantitative investigation is the lack of adequate techniques capable of control and real-time assessment of the transient and microscopic process of single-cell sonoporation. The inherently complex and highly dynamic nature of microbubble cavitation not only poses great difficulties to control sonoporation especially at the single-cell level but also renders an ensemble approach inadequate for probing the detailed processes of sonoporation deterministically.

Recently, several studies (7, 21, 22) addressed this challenge using various innovative approaches for generating and trapping a single microbubble to induce sonoporation of a single cell, but required complex laser systems for controlling bubbles and only worked with one cell at a time. No quantification of membrane poration and delivery was performed in these studies.

We have previously employed a voltage clamp technique to monitor sonoporation (23–26) in real time by measuring the transmembrane current (TMC) of single *Xenopus* oocytes. The ultrasound-induced localized membrane disruption allowed ions to flow nonselectively through the membrane, resulting in an increase of the TMC. The large diameter (approximately 0.8 mm) of *Xenopus* oocytes, a common membrane model for electrophysiological recordings (27), made recordings practical for these studies. However, cellular uptake corresponding to an increase of TMC was not measured in these cells, which are normally surrounded by a nontransparent vitelline membrane.

Patch clamp techniques have been used to study mammalian cells exposed to ultrasound in the presence of microbubbles (28, 29), but hyperpolarization of cells was related to the mechanical stress generated by microbubbles without assessment of membrane disruption.

Here, we targeted microbubbles to the plasma membrane of HEK-293 cells via specific ligand-receptor binding (Fig. 1*A*), and controlled sonoporation by tuning the pressure and timing of ultrasound pulses to selectively excite the cell-bound microbubbles. We measured and quantified the dynamic process of single-cell sonoporation and intracellular delivery using patch clamp recording, multiwavelength fluorescence microscopy, and high-speed bright field imaging (Fig. 1*B*). The detailed investigation of the sonoporation process reported here will help to develop sonoporation as an enabling technology for applications that require controlled cellular delivery of membrane-impermeant bioactive agents.

Results and Discussion

Different bubble concentrations for binding were used such that more than 65% of the cells in a monolayer culture bound to 1 or 2 bubbles (Fig. S1). This deterministic sonoporation environment allowed controlled interaction of membrane-bound microbubbles with individual cells and made it possible to carry out quantitative studies of sonoporation of single cells with high repeatability.

Author contributions: Z.F., H.L., M.M., and C.X.D. designed research; Z.F., H.L., and C.X.D. performed research; Z.F., H.L., and C.X.D. contributed new reagents/analytic tools; Z.F., M.M., and C.X.D. analyzed data; and Z.F., M.M., and C.X.D. wrote the paper.

The authors declare no conflict of interest.

This article is a PNAS Direct Submission.

[1]To whom correspondence should be addressed. E-mail: cxdeng@umich.edu.

This article contains supporting information online at www.pnas.org/lookup/suppl/doi:10.1073/pnas.1208198109/-/DCSupplemental.

www.pnas.org/cgi/doi/10.1073/pnas.1208198109

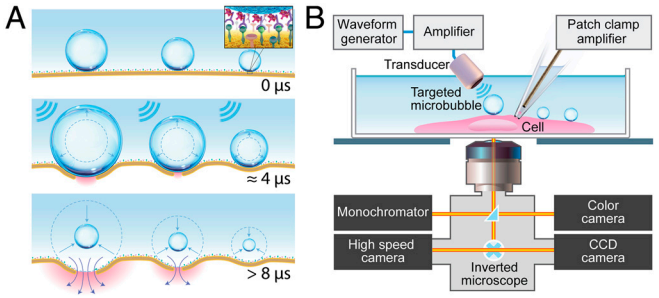

Fig. 1. (*A*) Ultrasound excitation of microbubbles attached to the cell membrane via receptor-ligand binding. Determined by their size, ultrasound-induced expansion and contraction of microbubbles generates transient membrane openings of different size, permitting transport of exogenous molecules into the cell cytoplasm. (*B*) Experimental setup for real-time assessment of single-cell sonoporation by ultrasound excitation of targeted microbubbles using synchronized simultaneous patch clamp recording, fluorescence imaging, and bright field videomicroscopy.

Threshold and Repeatability of Sonoporation. To measure sonoporation threshold, individual HEK-293 cells ($n = 8$) with one attached bubble (radius 2.6 ± 0.1 μm) were subjected to a single 8-μs ultrasound pulse after adding propidium iodide (PI) in the solution. By detecting the resulting intracellular fluorescence, we measured the acoustic pressure threshold for sonoporation of the HEK-293 cells to be 0.17 ± 0.05 MPa. Sonoporation occurred consistently [$n = 106$, fraction $f = 0.93$, with a 95% confidence interval ($CI_{95\%}$) of 0.86 to 0.97] when ultrasound pressure was above the threshold.

Ultrafast video microscopy revealed that sonoporation here was induced by inertial cavitation, where microbubbles expanded to more than twice their original radii and rapidly contracted (Fig. S2). Acoustic pressures below the threshold generated small oscillations of the bubbles (<10% of radius) and no sonoporation occurred ($n = 46$, $f = 0.96$, with a $CI_{95\%}$ of 0.86 to 0.99).

The Size and Resealing of Single Pores. To monitor sonoporation in real time, whole-cell recording in the presence of the membrane-impermeant dye PI was performed on single HEK293 cells under voltage clamp (−80 mV). Fig. 2 shows an example where a streptavidin-coated microbubble was attached to the cell membrane via biotinylated anti-CD51 antibodies, which bind to CD51 proteins on the cell surface. Before ultrasound application ($t < 0$ s), the absence of PI fluorescence (Fig. 2*B*) and TMC (Fig. 2*G*) confirmed cell membrane integrity. An ultrasound pulse (duration 2.4 μs, acoustic pressure 0.12 MPa) applied at $t = 0$ s excited the bubble and generated a rapid increase in the amplitude of the inward TMC (Fig. 2*G*), accompanied by PI fluorescence in the cell initiated from the location on the membrane where the attached bubble was excited (Fig. 2*C*). This location dependence indicated a localized membrane disruption that allowed the PI molecules to enter and bind to the RNA and DNA molecules in the cell cytoplasm, forming fluorescent PI–RNA or PI–DNA complexes. The resulting fluorescent complexes then diffused within the intracellular space (Fig. 2 *D* and *E*). Cell-viability assays based on calcein-AM performed after sonoporation showed that the cell was able to hydrolyze acetoxymethyl ester and retained the resulting calcein fluorophores, confirming recovery of the disrupted plasma membrane (Fig. 2*F*).

An ultrasound-induced increase in TMC was always accompanied by intracellular PI uptake from the location of the bubble attached to the membrane ($n = 10$, $f = 1$, with a $CI_{95\%}$ of 0.72 to 1.0). For cells that were sonoporated with PI uptake, simultaneous recording of TMC was successful in 10% of the cases ($n = 100$, $f = 0.1$, with a $CI_{95\%}$ interval of 0.06 to 0.18) because of the frequent loss of the gigaseal resistance between the membrane patch and the glass microelectrode.

From the maximal amplitude change of TMCs (5.6 ± 1.9 nA, $n = 4$) induced by ultrasound application, we estimated the maximum radius of a circular membrane disruption, or pore, to be 15.7 ± 2.6 nm, using a quasisteady electro-diffusion model (30) and the parameters listed in Table S1.

Although long-lived (e.g., >100 s) increases of TMC were observed (e.g., Fig. S3) in half of experiments ($n = 8$, $f = 0.5$, with a $CI_{95\%}$ of 0.21 to 0.79), we also recorded TMCs with faster and more regular recovery after sonoporation (Fig. 2*G*). We fit the shorter-lived TMC during recovery (0+ to 15 s) with $I(t) = I_{15} - I_f \exp(-k_f t) - I_s \exp(-k_s t)$, where I_{15} is the TMC value at 15 s (Fig. 2*H*), and determined the fast (k_f) and slow (k_s) time constants to be 4.21 ± 0.26 s^{-1} and 0.17 ± 0.05 s^{-1} with I_f and I_s of similar amplitude (3.2 ± 1.0 nA) ($R^2 = 0.92 \pm 0.05$). The slow time constant is similar to a previously measured value for *Xenopus* oocytes (0.11–0.21 s^{-1}), whereas the fast time constant is about four times that for *Xenopus* oocytes (0.79–1.19 s^{-1}) (25).

The existence of two distinctive recovery constants may reflect the different time scale of the mechanisms involved in cell membrane repair (31, 32), including extracellular Ca^{2+}-triggered homotypic membrane-fusion events that occur on a subsecond time scale, and facilitated self-sealing that is caused by reduction of membrane tension by exocytosis and believed to be associated with small membrane disruptions. The slow time constant may represent the relatively slow homotypic membrane fusion whereas the fast recovery constant may be associated with facilitated sealing, which is determined by the physical property of the specific membrane of each cell type.

The total net electric charge transported across the membrane, calculated from the temporal integration of the TMC, correlated linearly with the total PI fluorescence intensity (Fig. 2*I*), supporting diffusion-driven transmembrane transport of PI into the sonoporated cells.

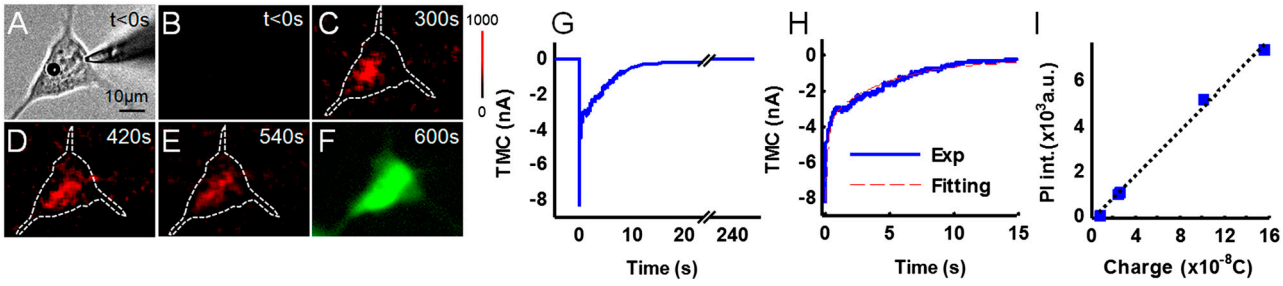

Fig. 2. (*A*) Whole-cell patch clamping of a HEK-293 cell with an attached bubble. (*B*) No intracellular PI fluorescence before ultrasound application (duration 2.5 μs, acoustic pressure 0.17 MPa). (*C–E*) Intracellular transport of PI induced by ultrasound excitation of the microbubble. (*F*) Postsonoporation calcein-AM assay showed retention of fluorescent calcein in the cell. (*G*) Rapid increase of the inward TMC induced by ultrasound excitation of the microbubble followed by a gradual recovery. (*H*) Fitting of the recovering TMC (0+ to 15 s) using a biexponential function. (*I*) Net electric charge transported across the membrane correlated with the intracellular PI fluorescence intensity.

The TMCs that exhibited long-lived elevated values could not be fit adequately by a biexponential function and were not included in the pore-size calculation reported here. Besides ultrasound-induced instability of the patch, these prolonged elevated values of TMC may reflect intrinsic variations in the cellular responses to mechanical injury of the heterogeneous cell membrane. Pinpointing the exact mechanisms may require analysis at a level of complexity beyond the scope of this study. In addition, the shallow depth of solution suitable for patch clamp recordings capped the ultrasound pressure that could be applied in our experiments because the perturbation of the air–liquid interface at elevated ultrasound pressures sometimes detached the recording microelectrode from the cell. Thus, the range of pore sizes measurable by patch clamp was limited in this study.

Despite these challenges, patch clamp recordings of sonoporation enabled real-time measurements of the submicron-scale events on the cell membrane as well as quantification of the pore size and recovery, parameters important for intracellular delivery. Spatiotemporally correlated patch clamp recording of an increase of TMC and fluorescence imaging of concomitant cellular uptake of membrane-impermeant molecules provided unequivocal evidence that ultrasound excitation of microbubbles generated membrane disruption.

Intracellular Transport and Intracellular Diffusion Coefficient. As shown in Fig. 3*A*, ultrasound excitation of cell-attached microbubbles readily generated localized and transient disruption of the cell membrane, allowing PI to enter the cell and form fluorescent PI–RNA or PI–DNA complexes. The gradual increase and stabilization of the total intracellular fluorescence intensity (Fig. 3*B*) indicated pore formation and resealing. With the assumption that the PI molecules entered the cytoplasm through a small circular hole on the membrane and rapidly bound to cytoplasmic DNAs and RNAs, we regarded it as a quasisteady-state diffusion problem and calculated the pore radius from the measured intracellular fluorescence intensity (*SI Text*). The pore in Fig. 3 was calculated to be 25.1 nm.

In addition, we treated the spatiotemporal evolution of intracellular fluorescence intensity after sonoporation as a 2D sourceless diffusion problem and obtained a closed-form solution that permitted calculation of the intracellular diffusion coefficient of the RNA or DNA (*SI Text*). From the measured spatiotemporal fluorescence intensity, which represented the diffusion of the PI–RNA/DNA complexes in the cell, we calculated the diffusion coefficient of the intracellular nucleic acids to be $(1.41 \pm 0.11) \cdot 10^{-9}$ cm^2 s^{-1} ($n = 4$; $R^2 = 0.8$), consistent with the reported diffusion coefficient of cytoplasmic RNA ($1 \cdot 10^{-9}$ cm^2 s^{-1}) (33). This method can be readily extended to measurement of intracellular diffusion coefficients of fluorescently labeled exogenous molecules by directly visualizing their transport in cells after sonoporation using time-lapse confocal fluorescence microscopy (34).

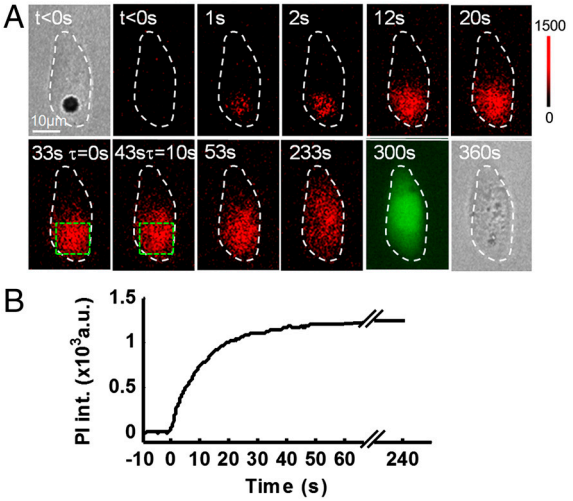

Fig. 3. Spatiotemporally localized intracellular delivery and diffusion coefficient. (*A*) Entry of PI into a HEK-293 cell induced by ultrasound excitation of a microbubble and subsequent spatiotemporal evolution of intracellular fluorescence. (*B*) Increase and stabilization of the total intracellular fluorescence intensity indicated pore formation and resealing. Ultrasound pulse duration was 8 μs and acoustic pressure amplitude was 0.17 MPa.

Spatiotemporally Controlled Delivery into Subcellular Regions. The response of a microbubble to ultrasound excitation depends on the size of bubbles and acoustic parameters (e.g., acoustic pressure and frequency) (20, 35). For the microbubbles (radius 1–3 μm) and ultrasound frequency (1.25 MHz) used in this study, higher acoustic pressures generated larger responses in bubbles with the same radius, and larger bubbles exhibited larger responses to the same acoustic pressure (Fig. S4 and Tables S2 and S3). Based on bubble sizes, ultrasound excitation can generate transient membrane openings of different size to control transport of exogenous molecules into the cell cytoplasm (Table S4).

By tuning the ultrasound application, we selectively excited microbubbles attached to different cells by applying ultrasound pulses with increasing acoustic pressure at different times to achieve spatiotemporally controlled sonoporation. Here, we present three examples.

Fig. 4*A* shows an example for spatially discriminated PI delivery within a single cell bound to two microbubbles (initial radius of 2.85 and 2.5 μm, respectively) at two different locations. Application of an ultrasound pulse (8 μs; 0.17 MPa) excited both bubbles and generated PI uptake from both locations, but the smaller bubble (blue arrow) generated less PI uptake than the larger bubble (yellow arrow). From the time-dependent PI fluorescence intensity within the cell after sonoporation, we calculated

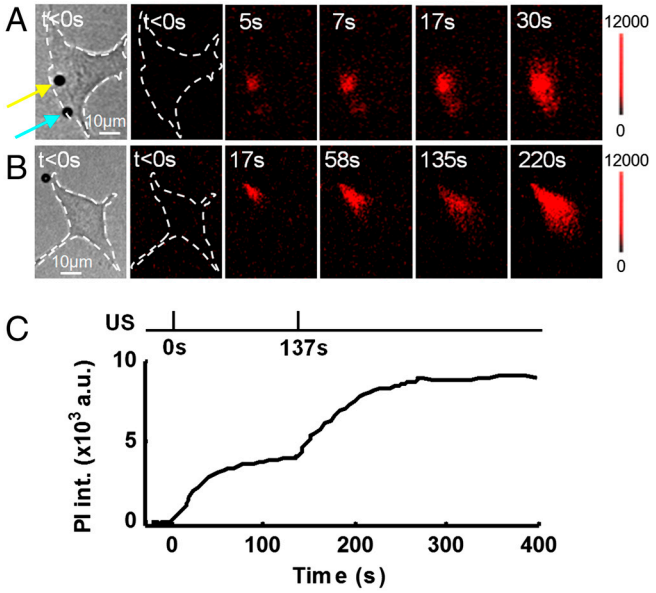

Fig. 4. Controlled ultrasound excitation of microbubbles and delivery in single cells. (*A*) Delivery of PI to subcellular locations by ultrasound excitation of microbubbles. The larger bubble (yellow arrow, radius 2.85 μm) generated more PI delivery in the cell than the smaller one (blue arrow, radius 2.5 μm). (*B*) Fluorescence imaging showing intracellular PI delivery by repeated ultrasound excitation of a microbubble at $t = 0$ and 137 s. (*C*) Total fluorescence intensity within the cell in *B* showing PI uptake generated by ultrasound application at $t = 0$ and 137 s. Ultrasound duration was 8 μs and acoustic pressure was 0.17 MPa.

the radii of pores to be 24.6 nm generated by the smaller bubble and 34.5 nm by the larger bubble (*SI Text*).

Fig. 4 *B* and *C* shows that repeated excitation of a microbubble (initial radius 2.25 μm) by ultrasound pulses (8 μs; 0.17 MPa) applied at 0 and 137 s resulted in two increases of PI in the cell. The corresponding radii of the pores were 18.8 and 20.4 nm for the two excitations, respectively.

Fig. 5 shows an example of selective delivery into different cells. The first ultrasound pulse (8 μs; 0.17 MPa) applied at $t = 0$ s delivered PI in cell 1 by collapsing the attached bubble (initial radius 2.5 μm) and generating a pore (radius 12.1 nm) without affecting the smaller bubble (radius 1.25 μm) attached to cell 2 (Fig. 5*A*). Excitation of bubble 2 and PI delivery into cell 2 were achieved by applying an ultrasound pulse ($t = 264$ s) with higher acoustic pressure (0.43 MPa) (Fig. 5*B*), which generated a pore with a radius of 19.6 nm.

The technique of tuning the ultrasound application to selectively excite microbubbles to control sonoporation should be applicable as a general delivery strategy for many impermeant agents of relevance (12–15) into selected individual cells with subcellular precision. This approach has the advantage that it requires no physical isolation of cells and/or specialized micron-scale fabrication and instrumentation, which are time-consuming and technically challenging.

Calcium Influx and Intercellular Calcium Waves Generated by Sonoporation of Targeted Cells. Sonoporation allowed diffusion-driven transport of ions across the otherwise highly selective cell membrane. As an important signaling ion, Ca^{2+} is tightly controlled in the cytosol at submicromolar (μM) concentration whereas the extracellular Ca^{2+} concentration ($[Ca^{2+}]_o$) is generally in the mM range. Thus, influx of extracellular Ca^{2+} into the cytoplasm is expected and observed in sonoporation because of the large concentration gradient across the cell membrane ($n = 80$, $f = 0.75$, with a $CI_{95\%}$ of 0.64 to 0.83).

In the example shown in Fig. 6, where three bubbles (B1, B2, and B3; initial radius 2.5, 2.0, and 1.5 μm) were attached to three cells (cells 1, 2, and 3), respectively, spatiotemporally controlled Ca^{2+} influx and calcium activities were induced by selective excitation of microbubbles using successive single ultrasound pulses with increasing acoustic pressure.

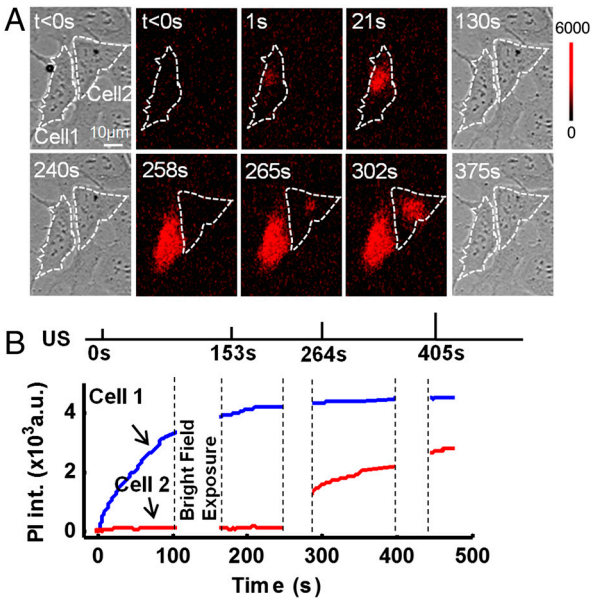

Fig. 5. Selective delivery in different cells. (*A*) Excitation of bubble 1 (radius 2.5 μm) and PI delivery in cell 1 by an ultrasound pulse (8 μs; 0.17 MPa; $t = 0$ s). Ultrasound pulses with pressures of 0.17 MPa ($t = 0$ s) or 0.26 MPa ($t = 153$ s) generated no PI delivery in cell 2. Ultrasound pulses with pressure of 0.43 MPa ($t = 264$ s) and 0.6 MPa ($t = 405$ s) excited bubble 2 (initial radius 1.25 μm) and generated PI uptake in cell 2. (*B*) Increase of total intracellular PI fluorescence by ultrasound applications.

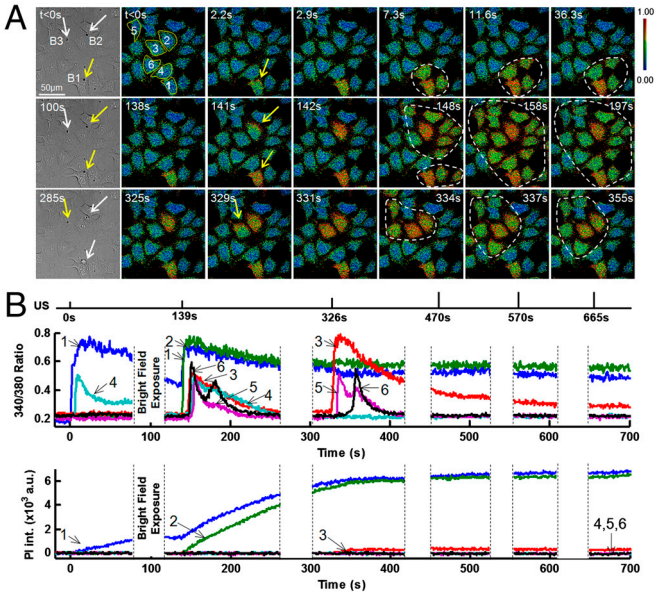

Fig. 6. Calcium influx and calcium wave generated by selective ultrasound excitation of microbubbles. (*A*, *Top*) Ultrasound pulse (2.4 μs; 0.17 MPa; $t = 0$ s) generated calcium influx only in cell 1 by bubble 1 (B1, radius 2.5 μm) and a delayed increase of $[Ca^{2+}]_i$ in neighboring cells (inside dashed circle). (*Middle*) Ultrasound pulse (2.4 μs; 0.26 MPa; $t = 139$ s) induced immediate increase of $[Ca^{2+}]_i$ in cells 1 and 2, and delayed $[Ca^{2+}]_i$ changes in surrounding cells, including oscillation of $[Ca^{2+}]_i$ in cell 6. (*Bottom*) Ultrasound pulse (2.4 μs; 0.43 MPa; $t = 326$ s) generated influx of calcium in cell 3 and calcium wave in surrounding cells including oscillation of $[Ca^{2+}]_i$ in cell 5. (*B*) Line plots showing changes in $[Ca^{2+}]_i$ and PI uptake generated by ultrasound pulses. Cells with immediate increase of $[Ca^{2+}]_i$ (cells 1, 2, and 3) had PI uptake, whereas the cells with delayed increase in $[Ca^{2+}]_i$ showed no PI uptake.

First, an ultrasound pulse with acoustic pressure of 0.17 MPa was applied at $t = 0$ s to excite only the largest bubble (B1) and reduce its radius to 2.0 μm, thereby generating immediate Ca^{2+} influx (Fig. 6*A*) and membrane disruption in cell 1, indicated by PI uptake in the cell (Fig. 6*B*). The radius of the pore based on PI fluorescence was calculated to be 2.1 nm. Delayed (approximately 7 s) increase of $[Ca^{2+}]_i$ in several neighboring cells (Fig. 6*A*, dashed circles in first row) that did not show PI uptake (Fig. 6*B*) indicated an intercellular Ca^{2+} wave after ultrasound application.

A second ultrasound pulse with higher pressure (0.26 MPa) was applied at $t = 139$ s to excite the smaller bubbles B2 and B1 (now both 2.0 μm) and reduce their radii to 1.25 μm, generating immediate Ca^{2+} influx in cell 2 and cell 1 with concomitant membrane disruption (PI uptake; Fig. 6*B*). The radii of the pores were 10.8 and 9.9 nm, respectively. Two calcium waves (Fig. 6*A*, dashed circles in the images at $t = 148$ s) followed the sonoporated cells in nearby surrounding cells. Oscillation of $[Ca^{2+}]_i$ in cell 6 indicated regulation of $[Ca^{2+}]_i$ by intracellular mechanisms.

A third ultrasound pulse with further increased pressure (0.43 MPa) applied at $t = 326$ s excited the smallest bubble, B3 (radius 1.25 μm), generating PI delivery and immediate Ca^{2+} influx in cell 3 with a pore of radius 3.7 nm, followed by a calcium wave in neighboring cells. Oscillation of $[Ca^{2+}]_i$ was observed in cell 5. Now that all bubbles were very small, no PI uptake and changes in $[Ca^{2+}]_i$ were generated by additional ultrasound pulses (0.43 MPa) (Fig. 6*B*).

Thus, sonoporation can generate spatiotemporally controlled increase of $[Ca^{2+}]_i$ in cells that were affected directly by micro-

bubble excitation (36–39), and in surrounding cells that were not sonoporated via calcium waves. The calcium waves were likely induced by factors released from the sonoporated cells (40, 41). Selective excitation of microbubbles to generate calcium signaling in single cells may be advantageous for investigating calcium signaling compared to conventional methods using glass-pipette mechanical stimulation or global exposure of cells to chemical agents.

Sonoporation-Mediated Delivery and Efflux of Calcein by Multidrug Resistance Protein-1 (MRP1). One of the challenges for studying the efflux of drug candidates and other xenobiotics out of cells is that some of these compounds require the presence of uptake pumps in order to become available as intracellular substrates for efflux pumps. In the absence of the appropriate uptake pump or alternative uptake mechanisms, substrates of efflux pumps sometimes cannot be recognized or can be mistakenly characterized as nonsubstrates.

We used sonoporation to deliver calcein as a fluorescent model compound of a membrane impermeant substrate of the MRP1 transporter protein (42, 43) in HEK-293 cells that overexpress MRP1 (HEK-MRP1) and in HEK-293 parental cells. Upon delivery we monitored calcein efflux and confirmed the cell viability by exposing the cells to PI 5 min after sonoporation. Ten min after ultrasound-induced delivery, the fluorescence intensity of calcein in HEK-293 parental cells that do not express MRP1 exhibited only a slight decrease (approximately 5%) (Fig. 7 *A* and *C*), as expected. In contrast, we observed approximately 40% decrease of fluorescence intensity in HEK-MRP1 cells in the same time period (Fig. 7 *B* and *C*). By fitting an exponential decay function to the calcein fluorescence intensities , we estimated an efflux rate of $(1.08 \pm 0.2) \cdot 10^{-4}$ s^{-1} ($n = 4$) for the HEK-293 parental cells and a rate of $(7.87 \pm 2.87) \cdot 10^{-4}$ s^{-1} ($n = 15$), approximately eight times faster, for HEK-MRP1 cells.

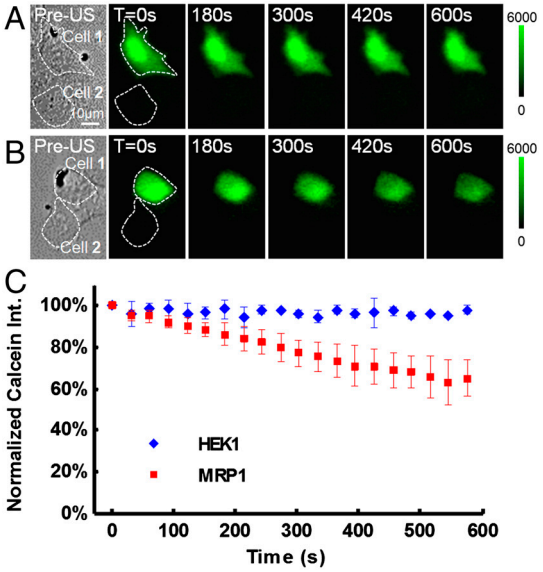

Fig. 7. Efflux of membrane-impermeant calcein after sonoporation delivery. (*A*) Sonoporation delivered calcein into a HEK-293 parental cell (cell 1), whereas cell 2, without attached microbubble, had no calcein uptake. Fluorescence intensity of calcein in cell 1 remained almost constant after sonoporation. (*B*) Sonoporation delivered calcein into a HEK cell that expressed multidrug-resistant protein 1 (HEK-MRP1) (cell 1), whereas cell 2 had no calcein uptake. After sonoporation, the fluorescence intensity of calcein in cell 1 decreased significantly. (*C*) Normalized intracellular calcein fluorescence intensity as function of time after sonoporation, showing significantly faster decrease in HEK-MRP1 cells ($n = 15$) than in HEK-293 parental cells ($n = 4$).

Therefore, controlled sonoporation can be readily used to evaluate the effect of intracellular substrates as well as codelivered molecules on transporter-induced efflux.

Conclusions

We demonstrated controlled single-cell sonoporation by selective ultrasound excitation of cell-attached microbubbles. Simultaneous real-time measurements using patch clamp recording and fluorescence imaging permitted quantitative assessment of single-cell sonoporation, such as the size and resealing rate of individual pores. We demonstrated spatiotemporally controlled calcium signaling and delivery of cell-impermeant molecules with subcellular precision, as well as unique use of controlled sonoporation-mediated delivery, including measuring the cytoplasmic diffusion coefficient of intracellular nucleic acids and the efflux of calcein by MRP1.

Future work will focus on delivery of biomolecules relevant to cellular functions to further develop sonoporation as a new tool for probing and manipulating the genetic, metabolic, and synthetic contents of selected single cells surrounded by neighboring cells, without exposing all cells to permeabilizing drugs that cause gross modification and complete disruption of processes and structures.

Materials and Methods

Cell Lines. Human embryonic kidney (HEK-293) cells (provided by Y. E. Chen, University of Michigan, Ann Arbor, MI) were grown in a humidified incubator at 37 °C and 5% CO_2 in DMEM supplemented with 10% FBS and 1% penicillin/streptomycin. HEK-293 cells transfected with the empty pcDNA3.1 vector (HEK-293 parental cells) and pcDNA3.1 vector containing ABCC1/MRP1 (HEK-MRP1 cells) (provided by S. V. Ambudkar, National Institutes of Health, Bethesda, MD) were maintained in a humidified incubator at 37 °C and 5% CO_2 in DMEM supplemented with 10% FCS, 1% penicillin/streptomycin, and G418 (0.8 mg/mL) (44). Cells were seeded in a glass-bottom Petri dish (MatTek) 1 day before experiments. Cell-viability assays were performed by incubating the cells with calcein-AM (1 μM; Invitrogen) at temperature 22–25 °C for 1–2 min in darkness before fluorescence imaging.

Microbubbles, Ultrasound, and Videomicroscopy. Targestar™-SA microbubbles (Targeson) were conjugated at room temperature to biotinylated anti-human CD51 antibody (Biolegend) in Dulbecco's PBS for 20 min, with a molar ratio of 10:2 for microbubbles ($5 \cdot 10^8$ mL^{-1}) and antibody (0.01 mg/mL). Then, 20-μL of the mixture was added in the cell-seeded dish immediately after removal of the medium. The dish was flipped upside down to allow the bubbles to float up to the cells to facilitate binding. After 10 min, unbound bubbles were removed by washing and the dish was refilled with Dulbecco's PBS for experiments.

An ultrasound transducer (1.25 MHz, diameter 1/4 inch; Advanced Devices), driven by a function generator (33250A; Agilent Technologies) and a power amplifier (75A250; Amplifier Research), was positioned at a 45° angle (to avoid the formation of standing waves and permit unobstructed microscopic imaging) with its active surface submerged in the medium 7 mm (Rayleigh distance) from the cells (Fig. 1*A*). The transducer was calibrated in free field in water using a calibrated 40-μm needle hydrophone (HPM04/1; Precision Acoustics). The acoustic pressure at the location of bubble/cell mentioned in this work accounted for reflection from the dish bottom.

A high-speed camera (Photron FASTCAM SA1; frame rate up to 200,000 frames/s) and an ultrafast camera (Specialized Imaging Multi-Channel Framing Camera SIM02; 2–4 Mframes/s) were used to monitor ultrasound excitation of microbubbles.

Patch Clamp Recording. Patch electrodes with resistances of 2.0–4.0 MΩ were fabricated from borosilicate glass using a P87 puller (Sutter Instruments). The pipette solution consisted of (in mM): 130 KCl, 2 $MgCl_2$, 10 Hepes, 2 ATP, and 0.2 GTP, with pH titrated to 7.2 using KOH. The bath solution consisted of (in mM): 140 NaCl, 5 KCl, 2 $CaCl_2$, 2 $MgCl_2$, 10 Hepes, and 5 glucose, with pH adjusted to 7.3 using NaOH. A single cell was voltage clamped (−80 mV) in a whole-cell configuration to record TMC using an Axonpatch 200B amplifier (Molecular Devices), with the whole-cell capacitance at 10–15 pF. Series resistance and membrane capacitance were compensated during recording. Data were digitized using an ITC-16 interface and Pulse 8.80 software (HEKA Instruments).

Fluorescence Microscopy. To detect cell membrane disruption, PI (668 Da, 100 μM; Sigma Aldrich) was added to the medium before ultrasound application. For ratiometric calcium imaging, cells were loaded with Fura2-AM by incubating with the dye for 60 min at 37 °C with Pluronic F-127 (0.05% vol/vol of 10% wt/vol) to facilitate intracellular loading. Extracellular Fura-2AM was removed by washing three times before experiments. For efflux measurements, calcein (100 μM; Invitrogen) was added before ultrasound application. After sonoporation, the cells were washed three times before fluorescence imaging.

A cooled CCD camera (Photometrics QuantEM), a monochromator with 5-nm bandpass (DeltaRAM X™; PTI), and a polychroic filter (73000v2; Chroma) were used for concurrent fluorescence imaging of PI and $[Ca^{2+}]_i$ (37). Pseudocolored ratio images of $[Ca^{2+}]_i$, based on the ratio of the emitted fluorescence intensities from 340- and 380-nm excitation, were created using MetaFluor Analyst (Molecular Devices) and MATLAB (Mathworks).

ACKNOWLEDGMENTS. This project was supported by National Institutes of Health Grants R01CA116592 (to C.X.D.) and R01GM081705 (to M.M.).

1. Luo D, Saltzman WM (2000) Synthetic DNA delivery systems. *Nat Biotechnol* 18:33–37.
2. Kootstra NA, Verma IM (2003) Gene therapy with viral vectors. *Annu Rev Pharmacol Toxicol* 43:413–439.
3. Torchilin VP (2006) Recent approaches to intracellular delivery of drugs and DNA and organelle targeting. *Annu Rev Biomed Eng* 8:343–375.
4. Hartwell LH, Hopfield JJ, Leibler S, Murray AW (1999) From molecular to modular cell biology. *Nature* 402:C47–C52.
5. Pines J (1999) Four-dimensional control of the cell cycle. *Nat Cell Biol* 1:E73–E79.
6. Tachibana K, Uchida T, Ogawa K, Yamashita N, Tamura K (1999) Induction of cell-membrane porosity by ultrasound. *Lancet* 353:1409.
7. Prentice P, Cuschieri A, Dholakia K, Prausnitz M, Campbell P (2005) Membrane disruption by optically controlled microbubble cavitation. *Nat Phys* 1:107–110.
8. Miller DL, Pislaru SV, Greenleaf JE (2002) Sonoporation:Mechanical DNA delivery by ultrasonic cavitation. *Somatic Cell Mol Genet* 27:115–134.
9. McCreery TP, Sweitzer RH, Unger EC, Sullivan S (2004) DNA delivery to cells in vivo by ultrasound. *Methods Mol Biol* 245:293–298.
10. Korpanty G, et al. (2005) Targeting of VEGF-mediated angiogenesis to rat myocardium using ultrasonic destruction of microbubbles. *Gene Ther* 12:1305–1312.
11. Newman CM, Bettinger T (2007) Gene therapy progress and prospects: Ultrasound for gene transfer. *Gene Ther* 14:465–475.
12. Hauff P, et al. (2005) Evaluation of gas-filled microparticles and sonoporation as gene delivery system: Feasibility study in rodent tumor models. *Radiology* 236:572–578.
13. Taniyama Y, et al. (2002) Development of safe and efficient novel nonviral gene transfer using ultrasound: Enhancement of transfection efficiency of naked plasmid DNA in skeletal muscle. *Gene Ther* 9:372–380.
14. Taniyama Y, et al. (2002) Local delivery of plasmid DNA into rat carotid artery using ultrasound. *Circulation* 105:1233–1239.
15. Taylor SL, Rahim AA, Bush NL, Bamber JC, Porter CD (2007) Targeted retroviral gene delivery using ultrasound. *J Gene Med* 9:77–87.
16. Vandenbroucke RE, Lentacker I, Demeester J, De Smedt SC, Sanders NN (2008) Ultrasound assisted siRNA delivery using PEG-siPlex loaded microbubbles. *J Controlled Release* 126:265–273.
17. Suzuki R, Oda Y, Utoguchi N, Maruyama K (2011) Progress in the development of ultrasound-mediated gene delivery systems utilizing nano- and microbubbles. *J Controlled Release* 149:36–41.
18. O'Brien WD, Jr (2007) Ultrasound-biophysics mechanisms. *Prog Biophys Mol Biol* 93:212–255.
19. Marmottant P, Hilgenfeldt S (2003) Controlled vesicle deformation and lysis by single oscillating bubbles. *Nature* 423:153–156.
20. Wu J, Nyborg WL (2008) Ultrasound, cavitation bubbles and their interaction with cells. *Adv Drug Delivery Rev* 60:1103–1116.
21. Zhou Y, Yang K, Cui J, Ye JY, Deng CX (2012) Controlled permeation of cell membrane by single bubble acoustic cavitation. *J Controlled Release* 157:103–111.
22. Sankin GN, Yuan F, Zhong P (2010) Pulsating tandem microbubble for localized and directional single-cell membrane poration. *Phys Rev Lett* 105:078101.
23. Deng CX, Sieling F, Pan H, Cui J (2004) Ultrasound-induced cell membrane porosity. *Ultrasound Med Biol* 30:519–526.
24. Zhou Y, Cui J, Deng CX (2008) Dynamics of sonoporation correlated with acoustic cavitation activities. *Biophys J* 94:L51–L53.
25. Zhou Y, Shi J, Cui J, Deng CX (2008) Effects of extracellular calcium on cell membrane resealing in sonoporation. *J Controlled Release* 126:34–43.
26. Pan H, Zhou Y, Izadnegahdar O, Cui J, Deng CX (2005) Study of sonoporation dynamics affected by ultrasound duty cycle. *Ultrasound Med Biol* 31:849–856.
27. Shi J, et al. (2002) Mechanism of magnesium activation of calcium-activated potassium channels. *Nature* 418:876–880.
28. Tran TA, Roger S, Le Guennec JY, Tranquart F, Bouakaz A (2007) Effect of ultrasound-activated microbubbles on the cell electrophysiological properties. *Ultrasound Med Biol* 33:158–163.
29. Tran TA, Le Guennec JY, Bougnoux P, Tranquart F, Bouakaz A (2008) Characterization of cell membrane response to ultrasound activated microbubbles. *IEEE Trans Ultrason Eng* 55:43–49.
30. Zhou Y, Kumon RE, Cui J, Deng CX (2009) The size of sonoporation pores on the cell membrane. *Ultrasound Med Biol* 35:1756–1760.
31. McNeil PL, Kirchhausen T (2005) An emergency response team for membrane repair. *Nat Rev Mol Cell Biol* 6:499–505.
32. McNeil PL, Miyake K, Vogel SS (2003) The endomembrane requirement for cell surface repair. *Proc Natl Acad Sci USA* 100:4592–4597.
33. Fusco D, et al. (2003) Single mRNA molecules demonstrate probabilistic movement in living mammalian cells. *Curr Biol* 13:161–167.
34. Paganin-Gioanni A, et al. (2011) Direct visualization at the single-cell level of siRNA electrotransfer into cancer cells. *Proc Natl Acad Sci USA* 108:10443–10447.
35. Ferrara K, Pollard R, Borden M (2007) Ultrasound microbubble contrast agents: Fundamentals and application to gene and drug delivery. *Annu Rev Biomed Eng* 9:415–447.
36. Kumon RE, et al. (2007) Ultrasound-induced calcium oscillations and waves in Chinese hamster ovary cells in the presence of microbubbles. *Biophys J* 93:L29–L31.
37. Fan Z, Kumon RE, Park J, Deng CX (2010) Intracellular delivery and calcium transients generated in sonoporation facilitated by microbubbles. *J Controlled Release* 142:31–39.
38. Park J, Fan Z, Kumon RE, El-Sayed ME, Deng CX (2010) Modulation of intracellular Ca^{2+} concentration in brain microvascular endothelial cells in vitro by acoustic cavitation. *Ultrasound Med Biol* 36:1176–1187.
39. Kumon RE, et al. (2009) Spatiotemporal effects of sonoporation measured by real-time calcium imaging. *Ultrasound Med Biol* 35:494–506.
40. Berridge MJ, Lipp P, Bootman MD (2000) The versatility and universality of calcium signalling. *Nat Rev Mol Cell Biol* 1:11–21.
41. Paemeleire K, et al. (2000) Intercellular calcium waves in HeLa cells expressing GFP-labeled connexin 43, 32, or 26. *Mol Biol Cell* 11:1815–1827.
42. Olson DP, Taylor BJ, Ivy SP (2001) Detection of MRP functional activity:Calcein AM but not BCECF AM as a Multidrug Resistance-related Protein (MRP1) substrate. *Cytometry* 46:105–113.
43. Hamilton KO, et al. (2001) Multidrug resistance-associated protein-1 functional activity in Calu-3 cells. *J Pharmacol Exp Ther* 298:1199–1205.
44. Muller M, et al. (2002) Evidence for the role of glycosylation in accessibility of the extracellular domains of human MRP1 (ABCC1). *Biochemistry* 41:10123–10132.